JOURNAL OF PROPULSION AND POWER
Vol. 26, No. 2, March–April 2010

Investigation of Rocket Exhaust Diffusers for Altitude Simulation

Hong-Gye Sung,* Hyo-Won Yeom,† Sangkyu Yoon,‡ Seong-Jin Kim,† and Jingon Kim*
Korea Aerospace University, Gyeonggi, 412-791, Republic of Korea

DOI: 10.2514/1.46226

The design and operational parameters of rocket exhaust diffusers equipped to simulate high-altitude rocket performance on the ground were investigated and characterized using a comprehensive approach (theoretical, numerical, and experimental). The physical model of concern includes a rocket motor, a vacuum chamber, and a diffuser, which have axisymmetric configurations. Further, the operational characteristics of a rocket exhaust diffuser were analyzed from a flow development point of view. Emphasis was placed on detailed flow structure in the diffuser, to observe the pressure oscillation in both the vacuum chamber and diffuser, which determines the minimum rocket-motor pressure required to start the diffuser. Numerical simulations were compared with experimental data on startup and in operational conditions to understand the effects of major design parameters, including the area ratio of diffuser to rocket-motor nozzle throat, the rocket-motor pressure, and the vacuum-chamber size.

Nomenclature

A_d	=	inner cross-sectional area of diffuser
A_{de}	=	exit cross-sectional area of diffuser
A_e	=	exit cross-sectional area of rocket nozzle
A_t	=	throat cross-sectional area of rocket nozzle
a_1, a_3, a_5	=	model constant of damping factor
C_f	=	friction coefficient
C_k	=	model constant of turbulent time scale
C_{ε^1}, C_{ε^2}	=	model constants of turbulent energy dissipation
C_μ	=	model constant of turbulent viscosity
c	=	speed of sound
E	=	specific total energy
F	=	force
f_μ	=	damping factor
h	=	specific enthalpy
k	=	turbulent kinetic energy
$(L/D)_d$	=	ratio of length to diameter of the diffuser
M	=	Mach number
M_t	=	turbulent Mach number
$\dot{m}$	=	mass flow rate
P	=	static pressure
P_a	=	ambient (atmospheric) pressure
P_c	=	vacuum-chamber pressure
P_e	=	exit pressure of diffuser
P_k	=	production of kinetic energy
P_o	=	total pressure of rocket motor
q_j	=	specific heat flux
R	=	specific gas constant
R_y	=	Reynolds number associated with vertical distance from the wall
T_t	=	total temperature
T_{turb}	=	turbulent time scale
t	=	time
u	=	velocity
x	=	spatial coordinate
y_n	=	vertical distance from the wall
α_1, α_2, α_3	=	model constants for compressible correction
γ	=	specific heat ratio
δ_{ij}	=	Kronecker delta
ε_c	=	compressible dissipation
ε_s	=	dissipation rate
μ	=	molecular viscosity
μ_t	=	turbulent viscosity
ν	=	kinematic viscosity
ρ	=	density
σ_k, σ_ε	=	model constants
τ_{ij}	=	viscous stress tensor
τ_k	=	Kolmogorov time scale

Subscripts

i, j, k	=	spatial coordinate index
st	=	starting condition
1, 2, 3	=	location in diffuser or model constant

Superscripts

$\bar{}$	=	time average
$\tilde{}$	=	Favre average
$''$	=	fluctuation associated with mass-weighted mean

Presented as Paper 0855 at the 46th AIAA Aerospace Sciences Meeting and Exhibit, Reno, NV, 7–11 Jan. 2008; received 3 July 2009; revision received 26 Sept. 2009; accepted for publication 27 Sept. 2009.

*Professor, School of Aerospace and Mechanical Engineering, Goyang. Member AIAA.

†Research Assistant, School of Aerospace and Mechanical Engineering, Goyang.

‡Research Assistant, School of Aerospace and Mechanical Engineering, Goyang; currently Hanwha Company, Ltd.

I. Introduction

A ROCKET motor designed to operate at high altitude needs a nozzle with a large expansion ratio to maximize thrust at much lower atmospheric pressure than that at sea level. These motors cannot be accurately tested on the ground because flow separation occurs in the nozzle. Therefore, to accurately evaluate the performance of such rocket motors, a test facility that replicates high-altitude conditions on the ground is required. In general, two kinds of test facilities are suggested: supersonic exhaust diffusers and ejectors. For simulated altitudes of around 20 km, the simplest method is the supersonic exhaust diffuser.

Ejectors are generally classified in two types: constant-pressure-mixing ejectors and constant-area-mixing ejectors. Keenan et al. [1] performed a comprehensive study on constant-pressure-mixing and constant-area-mixing ejectors. Fabri and Siestrunk [2] investigated the internal flow of constant-area-mixing supersonic ejectors at variable pressure ratios (ratio of stagnation pressure of primary flow

to backpressure) and different operating conditions. Emanuel [3] investigated steady-state supersonic ejector performance optimization assuming constant pressure mixing using the Rayleigh–Pitot formula. Lear et al. [4] studied two-phase flows and shock waves of an ejector system for a cooling system using Fabri choking.

Studies on testing methods, design methods, and the internal flow of diffuser systems simulating high-altitude conditions have been performed in research institutes, industries, and academic laboratories since the mid-1950s [5–12]. Experiments and theoretical analysis of various performance factors were performed to develop experimental equipment that can simulate high-altitude conditions on the ground [13–15]. Theoretical methods to determine the starting pressures of various types of diffusers (long cylindrical diffuser, long second-throat diffuser, short second-throat diffuser, etc.) were proposed [16–19]. For the design of a high-altitude test facility for testing the third-stage motor of a polar satellite launch vehicle, experiments using both cold nitrogen gas and hot rocket exhaust gas as driving fluids were carried out [20]. The high-altitude test facility (which consists of a vacuum pump, ejector, and diffuser) was developed to find an optimum configuration using numerical analysis to evaluate experimental data collected at the facility [21]. In the most recent research, a laboratory-scale high-altitude test facility was introduced to supply a hybrid rocket motor with an air-powered ejector and blowoff door for the initial lower backpressure [22].

For two decades, numerical investigations of internal shock structures and flow physics in the supersonic ejector/diffuser systems have been conducted [11,12,23,24]. These numerical studies have focused on the flow structure at steady state with minimal consideration of compressible turbulent effects. As the Mach number of a turbulent flow increases, the velocity fields can no longer be assumed to be solenoidal. Turbulent modeling for compressible flow therefore has to account for the additional correlations involving both the fluctuating thermodynamic quantities and the fluctuating dilatation. The interaction of a shock wave with a turbulent boundary layer leads to a significant increase in turbulence intensity and shear stress across the shock [25]. To account for the important features in high-speed flow, this study proposes a combined model of the low-Reynolds-number k-ε model [26] and the compressible dissipation and pressure dilatation proposed by Sarkar et al. [25], Sarkar [27], Dash and Kenzakowski [28], and Wilcox [29]. An unsteady numerical analysis is also performed to consider the unsteadiness of the flow structure as well as oscillatory vacuum-chamber pressure at the minimum startup and operating conditions.

For this paper, theoretical models (i.e., normal shock and momentum models) were employed and numerical simulations were compared with experimental data to investigate the effects of the major design parameters (which are the area ratio of diffuser to rocket-motor nozzle throat, vacuum-chamber size, and rocket-motor pressure) and thus to characterize startup and operational conditions.

II. Theoretical Models

The starting process of the supersonic exhaust diffuser can be explained through Fig. 1. In region 1, both the nozzle and diffuser are unstarted. The jet momentum exhausted from the rocket is not sufficient for the flow to fill the nozzle, and so the flow separates from the nozzle wall. As the pressure ratio P_0/P_a increases further, the nozzle flows full but overexpands, and yet the diffuser is still unstarted in region 2. The unstarted regime consists of two phases. In the first phase, the flow separates from the nozzle walls through an oblique shock, and in the second phase, the flow separation occurs at the nozzle exit. As the pressure ratio P_0/P_a further increases to the typical pressure ratio $(P_0/P_a)_{\text{st,min}}$, the diffuser also flows full so that the shock system is fully established in the duct. In this regime, the underexpanded supersonic jet from the nozzle impinges on the diffuser wall. At this stage, the supersonic exhaust diffuser is said to have started, and the corresponding pressure ratio is the minimum starting pressure ratio $(P_0/P_a)_{\text{st,min}}$. Previous research [15,16,20] has shown that two theoretical models based on normal shock and momentum theories can be used to predict the starting pressure. Whereas the normal shock model is simplest, the momentum model

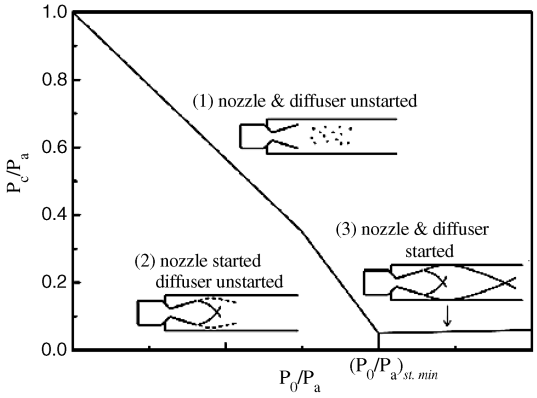

Fig. 1 Typical diffuser characteristic curve (Matsuo et al. [11]).

takes into account friction loss, which is not considered in the normal shock model.

A. Normal Shock Model

The basic concept of using a diffuser to simulate high-altitude conditions is to isolate the vacuum chamber surrounding a rocket from the atmosphere using a rocket jet's impingement on the diffuser wall connected to the vacuum chamber. The starting point is associated with the attachment of the jet at its location. The normal shock model stems from the fact that the overall consequence of the jet-impinging process in a long duct is closely approximated by a normal shock wave occurring at the inlet Mach number of the duct. The starting pressure ratio $(P_0/P_a)_{\text{st}}$ is then calculated by taking into account the static pressure recovery across the normal shock. Therefore, the starting pressure ratio $(P_0/P_a)_{\text{st}}$ is determined as if a normal shock wave were situated at the diffuser inlet.

Assuming that friction is neglected, total pressure is determined by the isentropic formulation for the area ratio A_d/A_t and a normal shock model for Mach number M_1 before the normal shock wave:

$$\frac{A_d}{A_t} = \frac{1}{M_1}\left[\frac{2}{\gamma+1}\left(1+\frac{\gamma-1}{2}M_1^2\right)\right]^{(\gamma+1)/2(\gamma-1)} \tag{1}$$

$$\frac{P_0}{P_1} = \left(1+\frac{\gamma-1}{2}M_1^2\right)^{\gamma/(\gamma-1)} \tag{2}$$

The pressure rise after a normal shock can be obtained from the normal shock theory, and the pressure at the diffuser exit can be obtained from the isentropic relation between station 2 (after a normal shock) and station 3 (diffuser exit) (see Fig. 2a):

$$\frac{P_2}{P_1} = \frac{2\gamma}{\gamma+1}M_1^2 - \frac{\gamma-1}{\gamma+1} \tag{3}$$

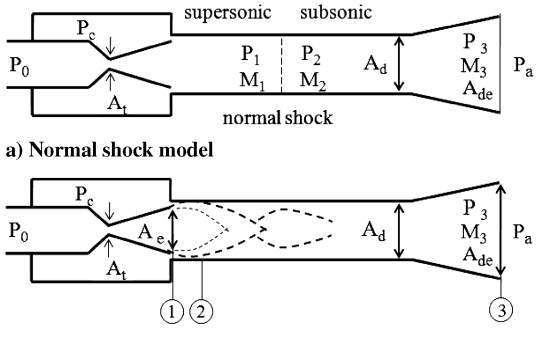

Fig. 2 Conceptual schematic of a diffuser.

$$M_2 = \sqrt{\frac{M_1^2 + \frac{2}{\gamma-1}}{\frac{2\gamma}{\gamma-1}M_1^2 - 1}} \tag{4}$$

Assuming that the diffuser exit pressure P_3 is equal to the atmosphere pressure P_a, the starting pressure ratio can be calculated from the following relation, which is a modified model that includes the expansion effect of the diffuser exit:

$$\left(\frac{P_0}{P_a}\right)_{\text{st}} = \left(\frac{P_0}{P_1}\right)\left(\frac{P_1}{P_2}\right)\left(\frac{P_2}{P_a}\right) = \frac{(1+\frac{\gamma-1}{2}M_1^2)^{\gamma/(\gamma-1)}}{\frac{2\gamma}{\gamma+1}M_1^2 - \frac{\gamma-1}{\gamma+1}}\left(\frac{1+\frac{\gamma-1}{2}M_3^2}{1+\frac{\gamma-1}{2}M_2^2}\right)^{\gamma/(\gamma-1)} \tag{5}$$

From the normal shock model, the starting pressure is a function of M_1, M_2, and M_3, determined by nondimensional geometry from A_d/A_t and A_{de}/A_d. Thus, it can be reasonably applied to experiments using scaled-down models.

B. Momentum Model

On starting, the free jet impinges upon the diffuser wall and then flows through a shock system to the exhaust (see Fig. 2b). The exhaust pressure at the start of the diffuser may be calculated by the 1-D conservation equation between the nozzle and the diffuser exit plane. The following assumptions are applied to simplify the solution of the conservation equations: 1) steady adiabatic flow, 2) perfect gas, 3) one-dimensional flow, 4) zero gas velocity in the test cell region, 5) linear Mach number distribution from jet impinge point (station 2 in Fig. 2b) to diffuser exit (station 3 in Fig. 2b) and a constant friction coefficient, and 6) static pressure at diffuser exit (station 3) that equals the exhaust pressure P_e.

These assumptions are used in a force balance between nozzle exit and jet impingement point, together with continuity and energy relations, as follows:

$$\frac{F_{\text{nozzle}} + P_c(A_d - A_e)}{\dot{m}\sqrt{RT_t}} = \frac{\sum_1^2 F}{\dot{m}\sqrt{RT_t}} = \frac{1+\gamma M_2^2}{M_2\sqrt{\gamma(1+\frac{\gamma-1}{2}M_2^2)}} \tag{6}$$

The summation of the force-mass relations between stations 1 and 3 (diffuser exit) can now be written as

$$\frac{\sum_1^2 F - \int_2^3 \mathrm{d}f_d}{\dot{m}\sqrt{RT_t}} = \frac{1+\gamma M_3^2}{M_3\sqrt{\gamma(1+\frac{\gamma-1}{2}M_3^2)}} \tag{7}$$

where the frictional force in the diffuser is $\mathrm{d}f_d = [(C_f P A_d \gamma M^2)/r_d]\,\mathrm{d}x$. By assuming a linear Mach number distribution from stations 2 (jet impingement point) to 3 (diffuser exit) and evaluating the integral, Eq. (7) may be rewritten as

$$\frac{\sum_1^2 F}{\dot{m}\sqrt{RT_t}} = \sqrt{\frac{2\gamma}{\gamma-1}}\frac{2C_f(L/D)_d}{M_3 - M_2}\left[\sqrt{\frac{2}{\gamma-1}+M_3^2} - \sqrt{\frac{2}{\gamma-1}+M_2^2}\right] + \frac{1+\gamma M_3^2}{M_3\sqrt{\gamma(1+\frac{\gamma-1}{2}M_3^2)}} \tag{8}$$

The maximum value of exhaust pressure at which a diffuser will start and operate can then be found from the conservation of mass:

$$P_3 = \dot{m}\sqrt{RT_t}\Big/\left[A_d M_3\sqrt{\gamma\left(1+\frac{\gamma-1}{2}M_3^2\right)}\right] \tag{9}$$

The starting pressure ratio is then calculated from Eq. (8):

$$\left(\frac{P_0}{P_a}\right)_{\text{st}} = \frac{P_0}{P_3} \tag{10}$$

III. Numerical Method

A. Governing Equation

The Favre-averaged governing equations based on the conservation of mass, momentum, and energy for a compressible flow can be written as

$$\frac{\partial\bar{\rho}}{\partial t} + \frac{\partial\bar{\rho}\tilde{u}_j}{\partial x_j} = 0 \tag{11}$$

$$\frac{\partial\bar{\rho}\tilde{u}_i}{\partial t} + \frac{\partial(\bar{\rho}\tilde{u}_i\tilde{u}_j + \bar{p}\delta_{ij})}{\partial x_j} = \frac{\partial(\bar{\tau}_{ij} - \overline{\rho u_j'' u_i''})}{\partial x_j} \tag{12}$$

$$\frac{\partial\bar{\rho}\tilde{E}}{\partial t} + \frac{\partial((\bar{\rho}\tilde{E}+\bar{p})\tilde{u}_j)}{\partial x_j} = \frac{\partial(\tilde{u}_i\bar{\tau}_{ij} - \overline{\rho h'' u_i''})}{\partial x_j} - \frac{\partial\bar{q}_j}{\partial x_j} \tag{13}$$

B. Turbulence Closure

The standard k-ε model, which was proposed for high-Reynolds-number flows, is traditionally used with a wall function and the variable y^+ as a damping function. However, the flow situation with separation has singularity on the wall because of y^+. Thus, a low-Reynolds-number k-ε model was developed for near-wall turbulence. Within certain distances from the wall, all energetic large eddies will reduce to Kolmogorov eddies (i.e., the smallest eddies in turbulence), and all the important wall parameters such as friction velocity, viscous length scale, and mean strain rate at the wall can be characterized by the Kolmogorov microscale.

Yang and Shih [26] proposed a time-scale-based k-ε model for the near-wall turbulence related to the Kolmogorov time scale as its lower boundary, so that the equation can be integrated to the wall. The advantages of this model are a) no singularity at the wall and b) adaptability to separation flow; since R_y instead of y^+ is used as the independent variable in the damping function, the model could be applicable in more complex flow. The low-Reynolds-number models have been designed to maintain the high-Reynolds-number formulation in the log-law region and further tuned to fit measurements for the viscous and buffer layers. The low-Reynolds-number model used in this work is based on Yang and Shih.

As the Mach number of a turbulent flow increases, the velocity fields can no longer be assumed to be solenoidal. Turbulence modeling for compressible flow has to account for the additional correlations involving both the fluctuating thermodynamic quantities and the fluctuating dilatation. The interaction of a shock wave with a turbulent boundary layer leads to a significant increase in turbulence intensity and shear stress across the shock [25]. To account for the important features of a high-speed flow, this study employs the combined model of compressible dissipation and pressure dilatation proposed by Sarkar et al. [25], Sarkar [27], Dash and Kenzakowski [28], and Wilcox [29] and the low-Reynolds-number k-ε model after validation. Low-Reynolds-number k-ε with Sarkar's model not only fairly predicted the impingement point of the jet on the diffuser wall and separation point compared with experiment data, but also captured dynamic motion near operational pressure [30].

The turbulent kinetic energy and its dissipation rate are calculated from the turbulence transport equations, written as follows:

$$\frac{\partial\bar{\rho}k}{\partial t} + \frac{\partial(\bar{\rho}\tilde{u}_j k)}{\partial x_j} = \frac{\partial}{\partial x_j}\left(\left(\mu + \frac{\mu_t}{\sigma_k}\right)\frac{\partial k}{\partial x_j}\right) + P_k - \bar{\rho}(\varepsilon_s + \varepsilon_c) + \overline{p''d''} \tag{14}$$

$$\frac{\partial\bar{\rho}\varepsilon_s}{\partial t} + \frac{\partial(\bar{\rho}\tilde{u}_j\varepsilon_s)}{\partial x_j} = \frac{\partial}{\partial x_j}\left(\left(\mu + \frac{\mu_t}{\sigma_\varepsilon}\right)\frac{\partial\varepsilon_s}{\partial x_j}\right) + \frac{(C_{\varepsilon 1}P_k - C_{\varepsilon 2}\bar{\rho}\varepsilon_s)}{T_{\text{turb}}} + \Lambda \tag{15}$$

where ε_c and $\overline{p''d''}$ represent compressible dissipation and pressure dilatation, respectively, and

$$\varepsilon_c = \alpha_1 M_t^2 \varepsilon_s \tag{16}$$

$$\overline{p''d''} = -\alpha_2 P_k M_t^2 + \alpha_3 \bar{\rho}\varepsilon_s M_t^2 \tag{17}$$

where $M_t^2 = 2k/c^2$ is the turbulent Mach number. The closure coefficients for the compressible corrections are

$$\alpha_1 = 1.0, \qquad \alpha_2 = 0.4, \qquad \alpha_3 = 0.2$$

In Eqs. (12) and (13), P_k, T_{turb}, and Λ are turbulent kinetic energy production rate, turbulent time scale, and damping function, respectively, and are represented as follows:

$$P_k = \left(\mu_t\left(\frac{\partial \tilde{u}_i}{\partial x_j} + \frac{\partial \tilde{u}_j}{\partial x_i} - \frac{2}{3}\frac{\partial \tilde{u}_k}{\partial x_k}\delta_{ij}\right) - \frac{2}{3}\bar{\rho}k\delta_{ij}\right)\frac{\partial \tilde{u}_i}{\partial x_j} \tag{18}$$

$$T_{\text{turb}} = \frac{k}{\varepsilon_s} + \tau_k, \qquad \tau_k = C_k\left(\frac{\nu}{\varepsilon_s}\right)^{1/2} \tag{19}$$

$$\Lambda = \nu\mu_t\left(\frac{\partial \tilde{u}_i}{\partial x_j \partial x_k}\right)^2 \tag{20}$$

where τ_k is the Kolmogorov time scale.

The turbulent viscosity and damping factor f_μ for the wall effect can be written as

$$\mu_t = \bar{\rho}C_\mu f_\mu k T_{\text{turb}}, \quad f_\mu = [1 - \exp(-a_1 R_y - a_3 R_y^3 - a_5 R_y^5)]^{1/2} \tag{21}$$

The damping factor is taken to be a function of $R_y = k^{1/2}y_n/\nu$.

The following constants are used:

$$\sigma_k = 1.0, \qquad \sigma_\varepsilon = 1.3, \qquad C_\mu = 0.09$$
$$C_{\varepsilon 1} = 1.44, \qquad C_{\varepsilon 2} = 1.92 \qquad a_1 = 1.5 \times 10^{-4}$$
$$a_3 = 5.0 \times 10^{-7}, \qquad a_5 = 1.0 \times 10^{-10}$$

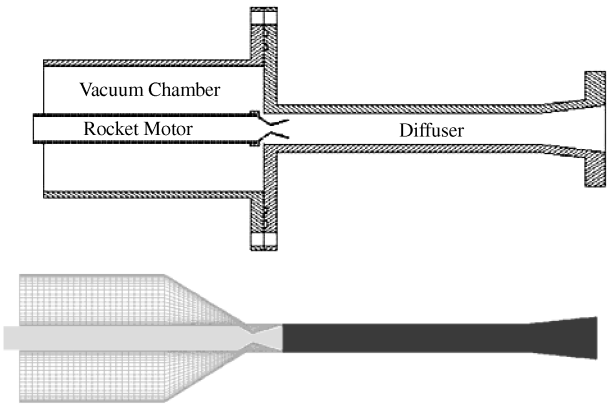

a) Large vacuum chamber

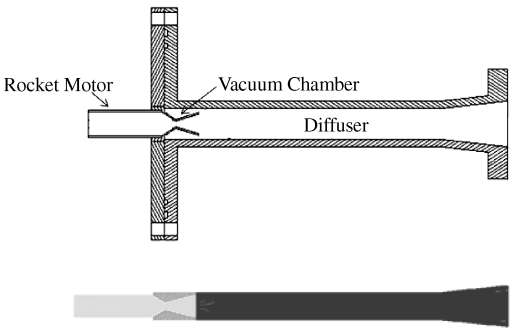

b) Small vacuum chamber

Fig. 3 Schematics and computational domains of diffusers: a) large vacuum chamber and b) small vacuum chamber.

C. Numerical Scheme

The conservation equations for moderate- and high-Mach-number flows are well-coupled, and standard numerical techniques perform adequately. In regions of low-Mach-number flows, however, the energy and momentum equations are practically decoupled and the system of conservation equations becomes stiff. Over the entire diffuser system, the flowfields are governed by a wide variety of time scales (from stagnation flow in the vacuum chamber to supersonic flow of the rocket exhaust jet). Such a wide range of time scales causes an unacceptable convergence problem. The authors determined that the conventional numerical scheme could not calculate the vacuum-chamber pressure accurately. To overcome this problem, we applied a two-step dual-time-integration procedure designed for all Mach number flows. First, a rescaled pressure term is used in the momentum equation to circumvent the singular behavior of pressure at low Mach numbers. Second, a dual-time-stepping integration procedure is established.

The pseudo time derivative may be chosen to optimize the convergence of the inner iterations by using an appropriate preconditioning matrix that is tuned to rescale the eigenvalues to render the same order of magnitude to maximize convergence. To unify the conserved flux variables, a pseudo time derivative of the form $\Gamma\partial Z/\partial\tau$ can be added to the conservation equation [31]. Because the pseudo-time-derivative term disappears upon convergence, a certain amount of liberty can be taken in choosing the variable Z. In this study, a pressure p' as the pseudotime derivative term in the continuity equation was introduced.

Whereas dual-time-stepping and lower/upper symmetric Gauss–Seidel are applied for second-order time integration, a control volume method is used to integrate inviscid fluxes represented by AUSMPW+ and MUSCL as well as viscous fluxes represented by

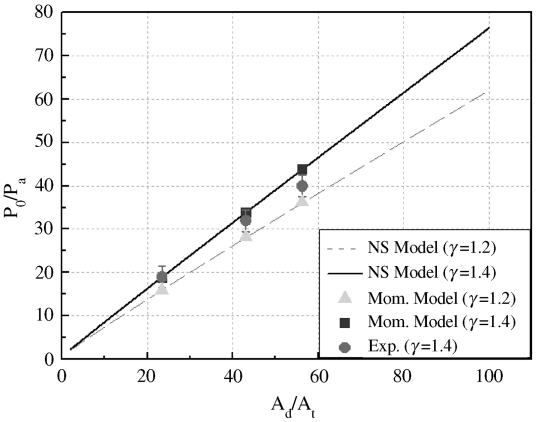

Fig. 4 Starting pressure ratio for the area ratio of diffuser to rocket nozzle throat.

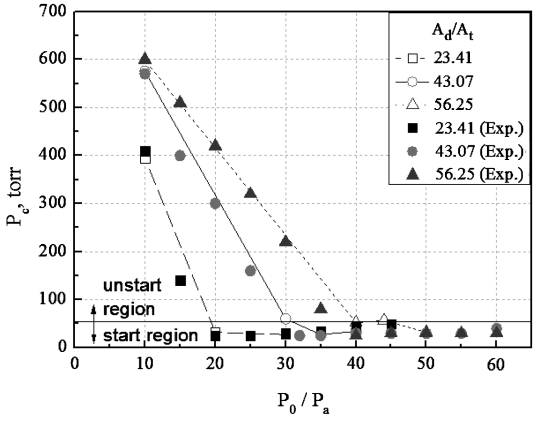

Fig. 5 Vacuum-chamber pressure versus rocket-motor pressure in the case of a large vacuum chamber.

Table 1 Dimensions of model diffusers

D_t, mm	A_e/A_t	A_d/A_t	L/D
	Large chamber, Fig. 3a		
2.8	35.02	56.25	12.38
3.2	26.81	43.07	12.38
4.34	14.58	23.41	12.38
	Small chamber, Fig. 3b		
4.34	14.58	23.41	12.38

central difference. A multiblock feature using a message-passing-interface library was used to speed up the calculation.

IV. Results and Discussion

A. Experiments

Two test models, one with a large vacuum chamber and the other with a small vacuum chamber, are illustrated in Fig. 3. Table 1 presents the dimensions of the model diffusers. The physical sizes of the test models were chosen to investigate the effect of major design parameters on diffuser start. The parameters of interest are the area ratio of the diffuser to the rocket nozzle throat (A_d/A_t), the expansion ratio of the rocket nozzle (A_e/A_t), and the rocket nozzle throat diameter. The stagnation pressure of the rocket motor was increased in 5-bar increments from 10 to 60 bar to investigate the effect of the starting pressure. Eight pressure transducers were installed: one in the vacuum chamber and seven along the diffuser [32]. Experiments using cold nitrogen gas ($\gamma = 1.4$) as a driving fluid were carried out.

B. Effect of Area Ratio of Diffuser to Rocket Nozzle Throat

Figure 4 shows the experimental results with the theoretically estimated values of the starting pressure ratio based on the normal shock model and the momentum model. Both results agree fairly well with the experiments. The starting pressure ratio $(P_0/P_a)_{st}$ increases as the area ratio of the diffuser to the rocket nozzle throat (A_d/A_t) increases. As the diffuser cross-sectional area becomes larger, the rocket-motor pressure should also be increased for the exhaust jet to fill the diffuser, because the motor pressure is linearly proportional to the mass flow rate of the jet exhausted from the rocket.

The higher the specific heat ratio γ, the greater the minimum starting pressure ratio $(P_0/P_a)_{st}$, which may motivate experiments using scaled-down models with cold nitrogen gas ($\gamma = 1.4$) as the driving fluid. Because the specific heat ratio of the rocket exhaust gas ($\gamma = 1.2$) is lower than that of the nitrogen gas, the actual starting pressure of the hot test turns out to be lower for the same A_d/A_t. That is, the actual supersonic exhaust diffuser would certainly start at the pressure determined by the cold-flow tests. This leads to the conclusion that model tests with cold flow are quite adequate to conservatively estimate the starting pressure of real-scale firing tests, as long as A_d/A_t remains the same. This is an important conclusion, given the high cost of full-scale hot firing tests in simulated high-altitude conditions on the ground.

Figure 5 shows the vacuum-chamber pressure versus rocket-motor pressure in the case of a large vacuum chamber; experimental values are marked as symbols and numerical results are represented by lines. The experimental and numerical values are comparable with each other. The vacuum pressure established by the rocket exhaust gas decreases as the rocket chamber pressure increases, and the decline rate of the pressure varies with A_d/A_t. It is recognized that the altitude, or simulated pressure, is controlled by the impingement of the exhaust jet on the wall of the diffuser inlet duct. The vacuum-chamber pressure of all cases that start are below 50 torr. However, even though the rocket-motor pressure is increased to over the starting pressure, the vacuum-chamber pressure does not further decrease and, in fact, remains almost the same. This reflects the importance of accurately predicting the starting pressure to appropriately and economically construct the test facility equipment.

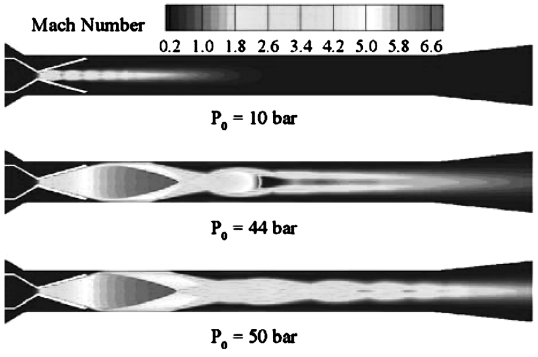

a) Mach number contours

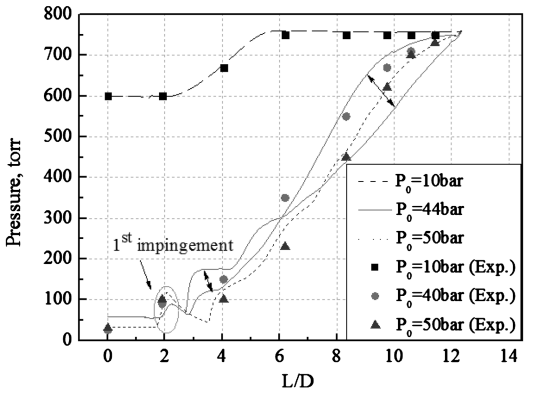

b) Pressure distribution

Fig. 6 Mach number contours zoomed in a diffuser and pressure distribution along the diffuser wall with $A_d/A_t = 56.25$ in the case of a large vacuum chamber (numerical data of 44 bar at t_0 and $t_0 + 4\Delta t$).

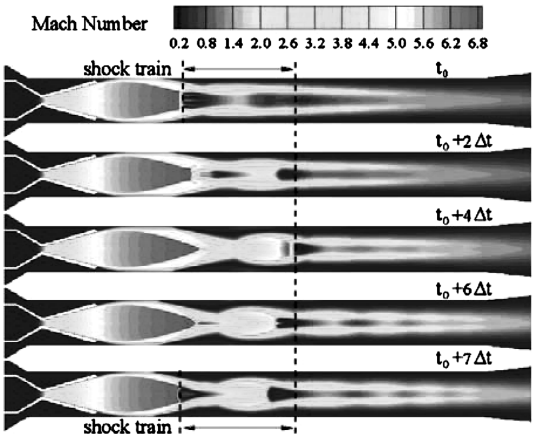

a) Mach number contours

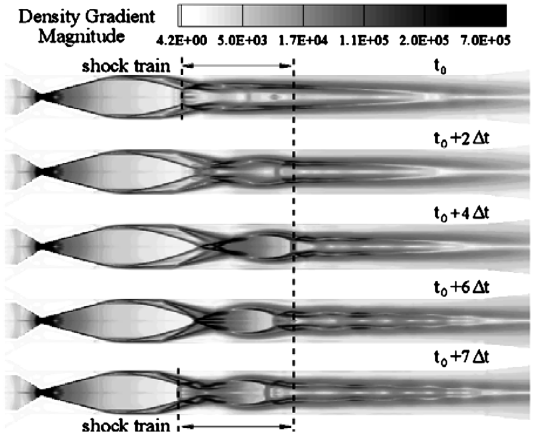

b) Density gradient magnitude

Fig. 7 Flow evolution in a diffuser at motor pressure 44 bar with $A_d/A_t = 56.25$ in the case of a large vacuum chamber ($\Delta t = 0.1$ ms).

C. Effect of Rocket-Motor Pressure

Figure 6a shows the Mach number contours for the case of the smallest nozzle throat area (highest expansion ratio $A_d/A_t = 56.25$) of the test models with a large vacuum chamber (see Table 1). Figure 3 shows the computational domains. The jet exhausted from the rocket nozzle impinges on the diffuser wall when the rocket-motor pressure increases to over 40 bar, which is around the starting pressure shown in Fig. 5. If the motor pressure increases further, the jet strength impinging on the diffuser wall also increases, as expected. Figure 6b describes the pressure distribution along the wall of the diffuser; experimental values are marked as symbols and numerical values are represented by lines. The values are in fairly good agreement. When the motor pressure is 10 bar (i.e., lower than the starting pressure), the pressure along the wall increases gradually to atmospheric pressure, because the flow in the diffuser is in the subsonic regime and the jet flow separates in the nozzle, as shown in Fig. 6a. At a motor pressure of 40 bar, the pressure rises after the impinging point and decreases in the expansion region, and finally rises at the exit of the diffuser. The experimental deviation of operational pressure at 40 bar is about ± 4 bar [31]. Numerical data at 44 bar of motor pressure more properly simulated the dynamic motion of a shock train in the diffuser [33]. The motor pressure at 50 bar provides two peaks of pressure, because the jet impinges on the diffuser wall twice.

At 44 bar of motor pressure near the starting pressure, the shock train was observed, as shown in Fig. 7. The small supersonic pocket behind the first shock diamond occurs at the axis of the diffuser, and it moves periodically downstream and upstream. The reason that the shock train accompanying pressure oscillation occurs in the diffuser is that the mass flux and momentum of exhaust jet are not enough to block out the pressure oscillation produced by acoustic-wave oscillation in the subsonic region behind the terminal shock. Thus, the shock train disappears if motor pressure increases up to 50 bar, producing a strong shock of exhaust jet, as shown in Fig. 6a. The period of oscillation may relate to the acoustic mode in the subsonic region after the first shock diamond. Thus, the vacuum-chamber pressure stays constant, but the pressure along the wall oscillates periodically with a certain amplitude, as shown in Fig. 6b. If the motor pressure decreases further, the shock train becomes weak. Figure 8 shows the flow evolution in a diffuser at a motor pressure of 40 bar. The flow structures represent different features, as shown in Figs. 7 and 8; whereas two shock pockets are generated at 44 bar, only one shock pocket is generated at 40 bar. In Figs. 7 and 8, t_0 was set at the moment that the terminal shock moves most upstream to the diffuser inlet. Figure 9 shows pressure distribution in the diffuser along the wall at motor pressures of 40 and 44 bar. The pressure-oscillation amplitudes and shapes of the two cases are different, because the mass flux and momentum of exhaust jet are different from each other. At the minimum starting pressure (40 bar), both the vacuum-chamber pressure and the wall pressure periodically oscillate due to the shock train. Somewhat above the starting pressure at 44 bar, however, the vacuum-chamber pressure oscillates negligibly, even though the wall pressure oscillates, as in the case of 40 bar (Fig. 9). The following phenomena may provide an explanation for why the vacuum chamber oscillates at 40 bar but remains almost constant at 44 bar. The observation of flow structures represented by the numerical shadowgraph (Fig. 10) shows the following:

1) At 44 bar, the cell end boundary of the shock diamond, i.e., the supersonic flow area, is further away from the nozzle exit than at 40 bar.

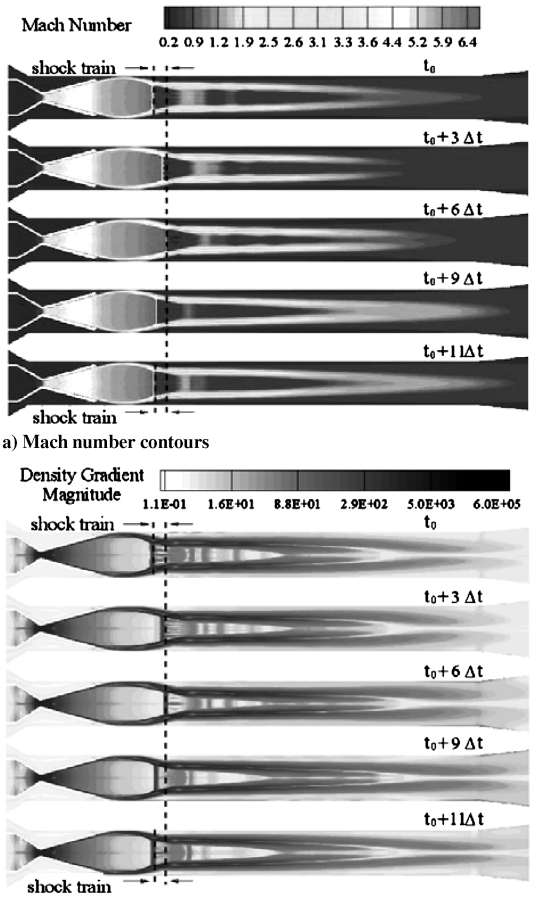

a) Mach number contours

b) Density gradient magnitude

Fig. 8 Flow evolution in a diffuser at motor pressure 40 bar with $A_d/A_t = 56.25$ in the case of a large vacuum chamber ($\Delta t = 0.1$ ms).

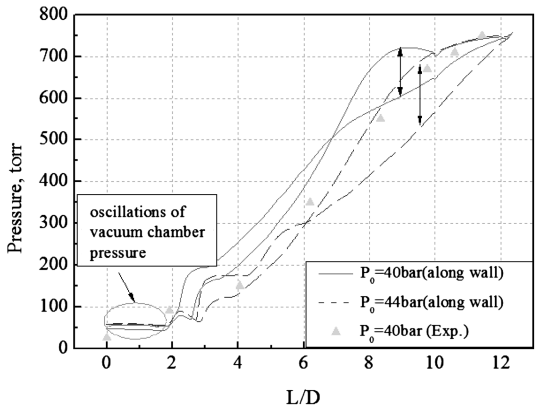

Fig. 9 Pressure distribution in the diffuser along the wall at motor pressures of 40 and 44 bar with $A_d/A_t = 56.25$ in the case of a large vacuum chamber (numerical data of 40 bar at t_0 and $t_0 + 6\Delta t$, and 44 bar at t_0 and $t_0 + 4\Delta t$.

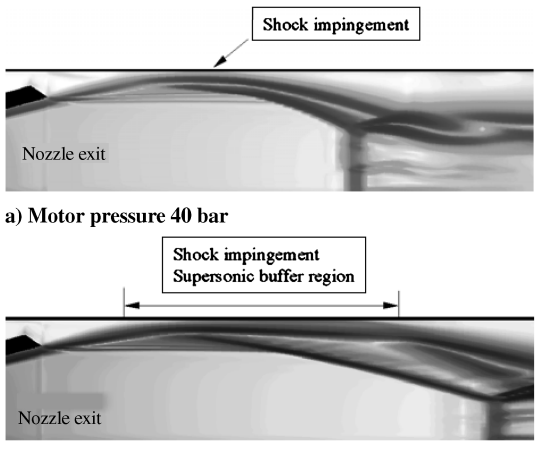

a) Motor pressure 40 bar

b) Motor pressure 44 bar

Fig. 10 Numerical shadowgraphs near shock impingement on the diffuser with $A_d/A_t = 56.25$ at motor pressure: a) 40 bar at t_0, and b) 44 bar at t_0.

2) The turbulent boundary layer at 44 bar surrounds the rocket exhaust.

Thus, the pressure oscillation behind the first shock diamond cannot penetrate into the vacuum chamber through the boundary layer because of attenuation in the large buffer region created by the turbulent boundary layer and the supersonic core at 44 bar.

D. Effect of Vacuum-Chamber Size

To investigate the effect of vacuum-chamber size, both experiments and numerical calculations were conducted using the same nozzle (i.e., $A_d/A_t = 23.41$) with different vacuum-chamber sizes: small and large. The volume ratio of the large vacuum chamber to the small vacuum chamber is about 129.4. Figure 11 shows the vacuum-chamber pressure P_c for small and large vacuum chambers. The experimental results and the numerical calculations are comparable, and vacuum sizes do not affect the starting pressure of the diffuser.

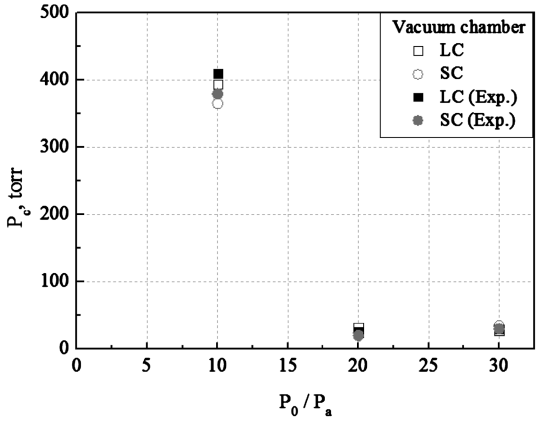

Fig. 11 Vacuum-chamber pressure for vacuum-chamber size.

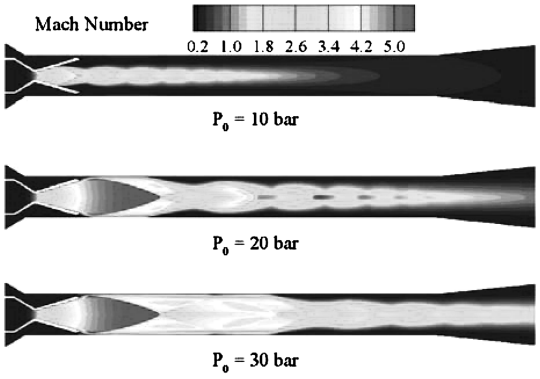

a) Mach number contours

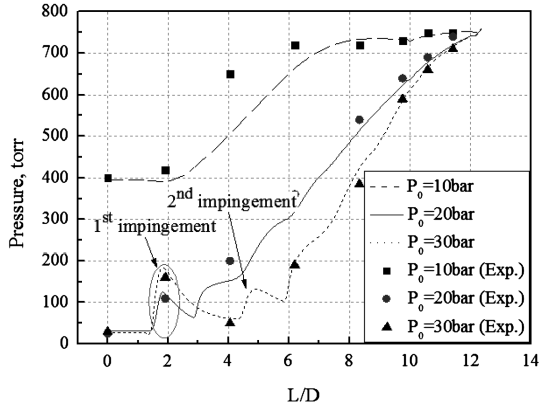

b) Pressure distribution

Fig. 12 Mach number contours in the diffuser and pressure distribution along the diffuser wall with a large vacuum chamber and A_d/A_t= 23.41.

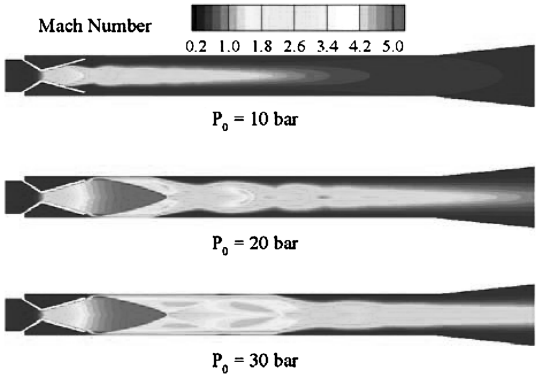

a) Mach number contours

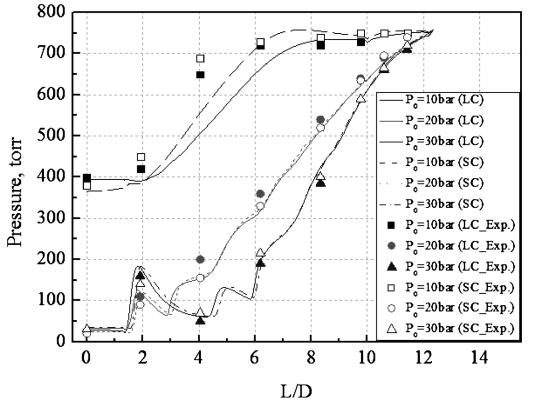

b) Pressure distribution

Fig. 13 Mach number contours in the diffuser with a small vacuum chamber and comparison of pressure distribution between two types of vacuum chambers with $A_d/A_t = 23.41$.

However, the transient time required to reach the steady state of the vacuum-chamber pressure increases as the size becomes larger, and so the rocket-motor size should be increased to supply enough exhaust gas to reach the steady state. Figures 12a and 13a represent the Mach number contours in the diffuser system with small and large vacuum chambers, respectively. In Figs. 12b and 13b, experiments in two different vacuum chambers are marked as symbols: solid symbols for the large vacuum chamber and open symbols for the small vacuum chamber. Numerical values are presented by a solid line for the large vacuum chamber and by a dotted line for the small vacuum chamber. The flow structures in the diffuser and the pressure distributions along the diffuser wall are very close if the diffuser starts. For both cases, the pressure in the vacuum chamber is below 50 torr, which is equivalent to an altitude of 20–25 km. The size of the vacuum chamber does not have much effect on the simulation altitude, but the transition time to reach at quasi-steady state in the case of a large vacuum chamber needs a longer time than that of a small chamber.

V. Conclusions

A comprehensive theoretical, numerical, and experimental approach was employed to study both the starting and operating conditions of supersonic exhaust diffusers. The results from the three approaches are quite comparable and convey valuable information for design and operational parameters of the diffuser, including specific heat ratio of exhaust gas, area ratio of diffuser to rocket nozzle, rocket-motor pressure, and vacuum-chamber size. The modified theoretical model based on shock wave and momentum theory is especially valuable for very quickly predicting the minimum starting pressure of the diffuser with acceptable accuracy. Numerical calculations using preconditions and a low-Reynolds-number k-ε turbulent model with compressible correction very precisely predict vacuum-chamber pressure, representing high-altitude conditions and identifying complex flow structures across a

very wide range of Reynolds numbers. Low-Reynolds-number k-ε with Sarkar's model not only fairly predicted jet impingement point and separation point compared with experiment data, but also captured dynamic motion at the starting pressure.

A certain pressure is required to start the diffuser, and the starting pressure increases as the area ratio of the diffuser to the rocket-motor nozzle (A_d/A_t) increases. The vacuum-chamber pressure remains almost the same, however, even though a rocket-motor pressure that is higher than the starting pressure is supplied. At the minimum starting pressure (40 bar), both the vacuum-chamber pressure and the diffuser wall pressure periodically oscillate due to the shock train. Somewhat above the minimum starting pressure at 44 bar, however, the oscillation of the vacuum-chamber pressure was negligible, even though the diffuser wall pressure oscillated as in the case at 40 bar, because of the large size of both the supersonic core and the turbulent boundary layer around the rocket exhaust at 44 bar. From the fact that the higher specific heat ratio requires a higher starting pressure, the supersonic exhaust diffuser using the rocket exhaust jet as a driving source would certainly start at the pressure simulated by cold-flow tests using nitrogen gas, because the specific heat ratio of the rocket exhaust gas is lower than that of nitrogen gas. Vacuum-chamber size does not affect the starting pressure of the diffuser, but the large chamber requires more time for the diffuser to reach a steady state.

Acknowledgments

This research was supported by Basic Science Program through the National Research Foundation of Korea funded by the Ministry of Education, Science and Technology (no. R0A-2007-000-10034-0). The authors would like to thank the Korea Aerospace Research Institute for partial funding through the research consortium of Korea Space Launch Vehicle.

References

[1] Keenan, J. H., Neumann, E. P., and Lustwerk, F., "An Investigation of Ejector Design by Analysis and Experiment," *Journal of Applied Mechanics*, Vol. 72, 1950, pp. 299–309.

[2] Fabri, J., and Siestrunk, R., "Supersonic Air Ejectors," *Advances in Applied Mechanics*, Vol. 5, edited by H. L. Dryden and T. von Kannan, Academic Press, New York, 1958, pp. 1–33.

[3] Emanuel, G., "Optimum Performance for a Single-Stage Gaseous Ejector," *AIAA Journal*, Vol. 14, No. 9, 1976, pp. 1292–1296. doi:10.2514/3.61462

[4] Lear, W. E., Sherif, S. A., and Steadham, J. M., "Design Considerations of Jet Pumps with Supersonic Two-Phase Flow and Shocks For Refrigeration and Thermal Management Applications," *International. Journal of Energy Research*, Vol. 24, No. 15, 2000, pp. 1373–1389. doi:10.1002/1099-114X(200012)24:15<1373::AID-ER662>3.0.CO;2-M.

[5] Annamalai, K., Visvanathan, K., Sriramulu, V., and Bhaskaran, K. A., "Evaluation of the Performance of Supersonic Exhaust Diffuser Using Scaled-Down Models," *Experimental Thermal and Fluid Science*, Vol. 17, No. 3, 1998, pp. 217–229. doi:10.1016/S0894-1777(98)00002-8

[6] Annamalai, K., Satyanarayana, T. N. V., Sriramulu, V., and Bhaskaran, K. A., "Development of Design Methods for Short Cylindrical Supersonic Exhaust Diffuser," *Experiments in Fluids*, Vol. 29, No. 4, 2000, pp. 305–308. doi:10.1007/s003489900071

[7] Sankaran, S., Satyanarayana, T. N. V., Annamalai, K., Visvanathan, K., Babu, V., and Sundararajan, T., "CFD Analysis for Simulated Altitude Testing of Rocket Motors," *Canadian Aeronautics and Space Journal*, Vol. 48, No. 2, 2002, pp. 153–162.

[8] Waltrup, P. J., and Billig, F. S., "Structure of Shock Waves in Cylindrical Ducts," *AIAA Journal*, Vol. 11, No. 10, 1973, pp. 1404–1408. doi:10.2514/3.50600

[9] Merkli, P. E., "Pressure Recovery in Rectangular Constant Area Supersonic Diffusers," *AIAA Journal*, Vol. 14, No. 2, 1976, pp. 168–172. doi:10.2514/3.61352

[10] Amatucci, V. A., Dutton, J. C., and Addy, A. L., "Pressure Recovery in a Constant-Area, Two-Stream Supersonic Diffuser," *AIAA Journal*, Vol. 20, No. 9, 1982, pp. 1308–1309. doi:10.2514/3.7977

[11] Matsuo, K., Miyazato, Y., and Kim, H.-D., "Shock Train and Pseudo-Shock Phenomena in Internal Gas Flows," *Progress in Aerospace Sciences*, Vol. 35, No. 1, 1999, pp. 33–100. doi:10.1016/S0376-0421(98)00011-6

[12] Chen, F., Liu, C. F., and Yang, J. Y., Supersonic Flow in the Second-Throat Ejector-Diffuser System," *Journal of Spacecraft and Rockets*, Vol. 31, No. 1, 1994, pp. 123–129. doi:10.2514/3.26411

[13] Sivo, J. N., Meyer, C. L., and Peters, D. J., "Experimental Evaluation of Rocket Exhaust Diffusers for Altitude Simulation," NASA TN-D-298, 1960.

[14] Goethert, B. H., "High Altitude and Space Simulation Testing," *ARS Journal*, 1962, pp. 872–882.

[15] Massier, P. F., and Roschke, E. J., "Experimental Investigation of Exhaust Diffusers for Rocket Engines," Jet Propulsion Lab., California Inst. of Technology, TR-32-210, Pasadena, CA, 1962.

[16] German, R. C., Bauer, R. C., and Panesci, J. H., "Methods for Determining the Performance of Ejector-Diffuser Systems," *Journal of Spacecraft and Rockets*, Vol. 3, No. 2, 1966, pp. 193–200. doi:10.2514/3.28418

[17] Wojciechowski, C. J., and Anderson, P. G., "Parametric Analysis of Diffuser Requirements for High Expansion Ratio Space Engine," NASA CR-161924, 1981.

[18] McAmis, R., and Bartlett, C., "Aerodynamic Free-Jet Nozzle Performance Augmentation Using an Exhaust Diffuser," AIAA Paper 91-2270, June 1991.

[19] Stephens, S. E., "Experimental and Computational Data from a Small Rocket Exhaust Diffuser," AIAA Paper 93-1860, June 1993.

[20] Annamalai, K., Visvanathan, K., Sriramulu, V., and Bhaskaran, K. A., "Evaluation of the Performance of Supersonic Exhaust Diffuser Using Scaled Down Models," *Experimental Thermal and Fluid Science*, Vol. 17, No. 3, July 1998, pp. 217–229. doi:10.1016/S0894-1777(98)00002-8

[21] Quebert, L., and Garcia, Y., "Theoretical and Experimental Design of an Exhaust Diffuser for an Upper Stage Engine of a Ballistic Missile," AIAA Paper 2001-3382, 2001.

[22] Otterstatter, M. R., Meyer, S. E., Heister, S. D., and Dambach, E. M., "Design of an Altitude-Testing Facility for Lab-Scale Propulsion Devices," AIAA Paper 2007-5323, 2007.

[23] Sankaran, S., Satyanarayana, T. N. V., Annamalai, K., Visvanathan, K., Babu, V., and Sundararajan, T., "CFD Analysis for Simulated Altitude Testing of Rocket Motors," *Canadian Aeronautics and Space Journal*, Vol. 48, No. 2, 2002, pp. 153–162.

[24] Bartosiewicz, Y., Aidoun, Z., Desevaux, P., and Mercadier, Y., "Numerical and Experimental Investigations on Supersonic Ejectors," *International Journal of Heat and Fluid Flow*, Vol. 26, No. 1, 2005, pp. 56–70. doi:10.1016/j.ijheatfluidflow.2004.07.003

[25] Sarkar, S., Erlebacher, B., Hussaini, M., and Kreiss, H., "The Analysis and Modeling of Dilatational Terms in Compressible Turbulence," *Journal of Fluid Mechanics*, Vol. 227, 1991, pp. 473–493. doi:10.1017/S0022112091000204

[26] Yang, Z., and Shih, T. H., "New Time Scale Based k-ε Model for Near-Wall Turbulence," *AIAA Journal*, Vol. 31, No. 7, 1993, pp. 1191–1197. doi:10.2514/3.11752

[27] Sarkar, S., "Modeling the Pressure-Dilatation Correlation," NASA Rept. 187566, May 1991.

[28] Dash, S., and Kenzakowski, D. C., "A Compressible-Dissipation Extension of the K-Epsilon Turbulence Model and Building-Block Data for its Validation," AIAA Paper 1992-2766, May 2992.

[29] Wilcox, D. C., "Effects of Compressibility," *Turbulence Modeling for CFD*, 2nd ed., DCW Industries, La Cañada, CA, 1998, Chap. 5.

[30] Yeom, H.-W., Kim, S.-J., and Sung, H.-G., "An Investigation of the Compressibility-Correction Turbulence Models in Supersonic Flow with Flow Separation," Korea Aerospace Univ., TM 07-003, Gyeonggi-do, ROK, 2007.

[31] Hsieh, S. Y., and Yang, V., "A Preconditioned Flux-Differencing Scheme for Chemically Reacting Flows at All Mach Numbers," *International Journal of Computational Fluid Dynamics*, Vol. 8, No. 1, 1997, pp. 31–49. doi:10.1080/10618569708940794

[32] Kim, Y., "Experimental Study on a Design of Diffuser for Simulating High-Altitude Environment," Korea Aerospace Research Inst., Daejeon, ROK, 2007.

[33] Yeom, H.-W., Yoon, S., and Sung, H.-G., "Flow Dynamics at the Minimum Starting Condition of a Supersonic Diffuser to Simulate a Rocket's High Altitude Performance on the Ground," *Journal of Mechanical Science and Technology*, Vol. 23, No. 1, 2009, pp. 254–261.

V. Yang
Associate Editor